Ultra-low dark current self-powered 0.36-1.7 μm broadband photodetector with tungsten oxide as interface modification layer

Qian Zhang[a,c], Libin Tang[b,c,*], Menghan Jia[a,c], Liqing Yang[b,c], Kar Seng Teng[d,*], and Yanfei Lü[a,*]

[a] *School of Physics and Astronomy, Yunnan University, Kunming 650500, People's Republic of China*

[b] *Kunming Institute of Physics, Kunming 650223, People's Republic of China*

[c] *Yunnan State Key Laboratory of Advanced Photoelectric Materials and Devices, Kunming 650223, People's Republic of China*

[d] *Department of Electronic and Electrical Engineering, Swansea University, Bay Campus, Fabian Way, Swansea SA1 8EN, United Kingdom*

E-mail: scitang@163.com, k.s.teng@swansea.ac.uk, optik@sina.com

Abstract

Lead sulfide colloidal quantum dots (PbS CQDs) exhibit tunable infrared bandgaps via quantum confinement but suffer from trap states predominantly localized on {100} facets, which severely degrade device performance in large CQDs due to increased facet exposure. Addressing the persistent challenge of fabricating high-quality large CQD films (>1.7 μm exciton peak), we developed a solution-phase exchange method to synthesize defect-controlled PbS CQDs. Furthermore, a self-powered p-i-n photodetector integrating a WOx interfacial modification layer was engineered. The WOx layer enhances contact quality at the metal electrode/PbS CQD film interface, achieving an ultra-low dark current density of 4.54 nA·cm^{-2} at -0.5V. Then, the device demonstrates excellent responsivity and detectivity across a broad range of illumination wavelengths, from 0.36 μm to 1.7 μm. Notably, the device achieves an exceptional detectivity for infrared light at 1.7 μm, exceeding 10^{10} Jones. These findings pave the way for designing and developing novel device structures for high-performance infrared photovoltaic detectors with extended wavelength capabilities.

Keywords: Self-powered; PbS colloidal quantum dots; low dark current; p-i-n heterojunction; broadband

1. Introduction

Colloidal quantum dots (CQDs) have garnered significant attention as promising materials for optoelectronic conversion due to their size-tunable bandgap, multiple exciton effects, and the potential for low-cost solution-based fabrication [1-5]. Among these, lead sulfide (PbS) CQDs are particularly notable for their impressive stability

and high absorption rates, establishing them as key contenders in the development of high-performance, cost-effective infrared photodetectors [6, 7]. However, the strong surface effects encountered immediately after synthesis can diminish the stability of these CQDs [8]. In the past, researchers have passivated the unsaturated dangling bonds on the surface of synthesized CQDs using long-chain organic ligands, such as oleylamine and oleic acid. While effective at passivation, these long-chain ligands increase the inter-particle distance, which reduces carrier transport efficiency. Moreover, as the size of the CQDs increases, a greater number of {100} facets, which are difficult to passivate, become exposed [9]. This exposure makes the CQDs prone to hydrolysis and instability in atmospheric environment. Additionally, due to the constraints of growth conditions, controlling surface defects through crystal-facet control in large-sized CQDs remains challenging. [10-12].

The engineering of ligand passivation on the surfaces of CQDs is crucial for fabricating high-quality PbS CQDs film [13, 14]. Substantial evidence indicates that various ligands can influence the positions of the conduction band, valence band, and the Fermi level of CQDs [15]. For example, PbS CQDs treated with 1,2-Ethanethiol (EDT) often exhibit p-type semiconductor behavior with the Fermi level positioned near the top of the valence band. In contrast, treatment with halide ions (TBAI, PbI_2, $PbBr_2$, and EMII) can induce a shift toward n-type characteristics, shifting the Fermi level toward near the bottom of the conduction band. Recent findings revealed that using halide ions for ligand exchange not only replaces long-chain ligands on the CQDs surface with shorter-chain alternatives but also effectively passivates surface defects. This process significantly enhances the quality of film formation using CQDs ink through solution-phase exchange as compared to solid-phase exchange methods, thereby consequently boosting device performance [8, 16]. However, halide-passivated CQDs need to be redispersed in highly polar solvents. The kinetics of the interaction between the CQDs surface and polar solvents, the stability of CQDs in polar solvents after halide passivation, and the large-scale preparation of thin-film devices using solution-phase methods remain extremely challenging [17]. Moreover, Ohmic contact formation at the metal electrode/PbS CQD film interface inherently generates injection currents due to interfacial trap states, work function mismatch, and defects within the quantum dot matrix. These currents constitute a fundamental component of dark current that can be minimized through interfacial engineering but cannot be fully eliminated, as dictated by thermodynamic equilibrium constraints at metal-semiconductor junctions.

Herein, we developed a mixed ligand passivation approach using PbI_2, $PbBr_2$, and $PbCl_2$ for PbS CQDs with an exciton peak at 1.7 μm (E_g = 0.73 eV), resulting in high-quality PbS CQDs films with significantly reduced surface defects. By incorporating WO_x as an ultra-thin interface modification layer, we developed a novel p-i-n photovoltaic self-powered broadband photodetector based on WO_x/0.9PbS-EDT/1.7PbS-X/ZnO/ZnO-NPs (0.9PbS-EDT: PbS CQDs with an exciton peak at 0.9 μm treated with EDT ligands; 1.7PbS: PbS CQDs with an exciton peak at 1.7 μm; X: Cl,Br,I; NPs: nanoparticles;). The device exhibits exceptional responsivity and detectivity across a broad spectrum, from ultraviolet to short-wave infrared, at room temperature. Remarkably, the device achieves a detectivity for infrared light at 1.7 μm

exceeding 10^{10} Jones, providing a robust foundation for the development of high-performance infrared photovoltaic detectors with extended wavelength capabilities.

2. Experimental

2.1. Materials

Gold target (Au, 99.999 %), tungsten target (W, 99.999 %), indium tin oxide target (ITO, 99.99 %) and zinc oxide target (ZnO 99.99 %) were purchased from Zhongnuo Advanced Material (Beijing) Technology Co., Ltd. Lead chloride ($PbCl_2$, 99.9 %), lead bromide ($PbBr_2$, ≥ 98 %), lead iodide (PbI_2, 99 %), and oleylamine (OLA, Tech. grade, 70 %) were purchased from Sigma-Aldrich. Oleic acid (OA, Tech. grade, 90 %), 1-octadecene (ODE, Tech. grade, 90 %), 1,2-ethanedithiol (EDT, 98 %), $Zn(Ac)_2 \cdot 6H_2O$ (99.99 %), KOH (99.99 %), NaAc (99.99 %), N-butylamine (99.5 %), and hexylamine (≥98 %) were purchased from Aladdin. Methanol (≥99.7 %), dimethylformamide (DMF, 99.5 %), ethanol (≥99.7 %) and octane (≥98.0 %) were purchased from Tianjin Zhiyuan Chemical Reagent Co., LTD. All the chemicals were used as received.

2.2 Synthesis and ligand exchange of PbS CQDs

The synthesis of 0.9PbS CQDs and 1.7PbS CQDs was achieved through cation exchange from ZnS nanorods, as reported by Yong Xia et al [18]. The process for the solution-phase ligand exchange of 1.7PbS CQDs was conducted within a N_2-filled glove box. Initially, a ligand solution comprising PbI_2:$PbBr_2$:$PbCl_2$ and NaAc was prepared with 10 mL DMF in a molar ratio of PbI_2:$PbBr_2$:$PbCl_2$:NaAc of 5:4:5:4. An equal volume of 10 mg/mL CQDs solution in n-octane was then prepared. The two solutions were then mixed and shaken vigorously for 1 min, followed by centrifugation at 7850 rpm for 2 min. The resulting precipitate was washed twice with n-octane. The secondary ligand solution was prepared using the first ligand solution. First, sodium acetate was removed by diluting the first ligand solution tenfold in 10 ml of DMF, to which 10 μL of hexylamine and 10 μL of n-butylamine were added, followed by thorough mixing. This solution was then introduced to the CQDs, which had been centrifuged after the first ligand exchange. After resting for 1 min, the mixture was shaken, and an equal volume of ethyl acetate was added as a counter-solvent before centrifuging again. The product was dried for 3 min and subsequently dissolved in a solution of N-butylamine, hexylamine, and DMF in a volume ratio of 8:1:6 at a concentration of 460 mg/mL. Continuous stirring for 30 min resulted in the formation of the CQDs ink (1.7PbS-X).

2.3 Device fabrication

The quartz substrate was boiled and washed in a mixture of ammonia, hydrogen peroxide, and deionized water at 80 °C for 30 min, followed by nitrogen blow-drying to prepare it for use. The bottom electrode, composed of Au, was prepared by magnetron sputtering onto the quartz substrate. Subsequently, the tungsten oxide thin film as an interface modification layer was deposited by sputtering a W target, using sputtering power of 100 W with oxygen to argon ratio of 1:3 for a duration of 60 s. A 0.9PbS CQDs layer was then spin-coated onto the tungsten oxide surface at a rotation speed of 1500 rpm. This was followed by an EDT ligand-exchanged process for 30 s,

after which the exchanged quantum dots were thoroughly washed three times with methanol. This process was repeated three times resulting in the formation of the 0.9PbS-EDT film through a layer-by-layer technique. The subsequent layer, 1.7PbS-X, was deposited via spin coating of the CQDs ink at 1500 rpm for 30 s on top of the 0.9PbS-EDT film. ZnO-NPs were synthesized using the hot injection method as reported by Zhang et al [19]. The synthesized ZnO-NPs were dissolved in a solvent mixture of DMSO and chloroform and were spin-coated onto the 1.7PbS-X layer at 5000 rpm for 60 s. This layer serves to protect the underlying CQDs in the light-absorbing layer during the sputtering of the ZnO electron transport layer. Finally, the ZnO electron transport layer and the top ITO electrode were deposited by the sputtering technique. The effective area of the device was 0.09 cm^2.

2.4 Characterization

The deposited films (e.g., WO_x, 1.7PbS-X, 0.9PbS CQDs and ZnO) were characterized using UV-Vis spectroscopy (iHR-320), ultra-violet photoelectron spectroscopy (UPS, ESCALAB Xi^+) with He-I excitation source (21.22 eV), X-ray photoelectron spectroscopy (XPS, K-$Alpha^+$) with a monochromatic Al Kα radiation source (1486.6 eV), X-ray diffraction (XRD, EMPYREAN), transmission electron microscope (TEM, JEM-2100), atomic force microscope (AFM, SPA-400) and scanning electron microscope (SEM, Hitachi S-3400N).

Current-voltage (*I-V*) and transient response (*I-t*) measurements on the photodetectors were performed using a Keithley 2400 source meter. The *I-t* measurements were carried out with LED driven by function/arbitrary waveform generator (RIGOL, DG 1022U). Noise power spectrum (i_n) testing was performed using a noise spectrum analyzer. All measurements were conducted at room temperature.

3. Results and discussion

A low-resolution TEM image of the synthesized 1.7PbS CQDs via cation exchange from ZnS nanorods, as reported by Zhang et al [18], is shown in Fig. 1(a). Fig. 1(b) shows a TEM image of 1.7PbS-X CQDs. Notably, the distance between the 1.7PbS CQDs decreases following solution-phase ligand exchange. The corresponding high-resolution TEM (HRTEM) image of a single 1.7PbS-X CQD is shown in Fig. 1(c). The image reveals lattice fringes of PbS, indicating that the synthesized CQDs are well crystallized after ligand passivation and exhibit no visible surface defects. The figure displays two types of lattice fringes with lattice spacing of 0.297 nm and 0.211 nm, corresponding to the (200) and (220) facets of PbS crystals, respectively. The inset of Fig. 1(c) presents the electron diffraction pattern. Size analysis based on the TEM image indicates that the synthesized CQDs have an average particle size of approximately 7.73 nm (as shown in Fig. 1(d)), which is consistent with the findings of Zhang et al. SEM images, including an enlarged view of the 1.7PbS-X CQDs film, are shown in Fig. 1(e). The surface of the 1.7PbS-X CQDs film is smooth and flat, and the dense, high-quality film provides an excellent foundation for the subsequent preparation of high-performance devices. Fig. 1(f) illustrates the crystal structure of PbS. The XRD patterns of the 1.7PbS CQDs film and 1.7PbS-X CQDs film on quartz substrates matches the PbS standard PDF card (JCPDS# 05-0592), which are shown in Fig. 1(g). it can be

found that after halide ligand passivation, the peak intensity ratio of {111} facets in 1.7PbS-X CQDs is significantly reduced. Compared to the original 1.7PbS CQDs, the peak intensity ratio between {100} facets and {111} facets is more closely match the intensity ratio in the PbS standard PDF card. This indicates that the mixed-ligand solution-phase exchange strategy results in the ordering of the crystal structure of PbS due to effective suppression. AFM images, along with a 3D representation of the 1.7PbS-X CQDs film, are displayed in Fig. 1(h) and (i), revealing a measured root-mean-square (RMS) surface roughness of 4.1 nm.

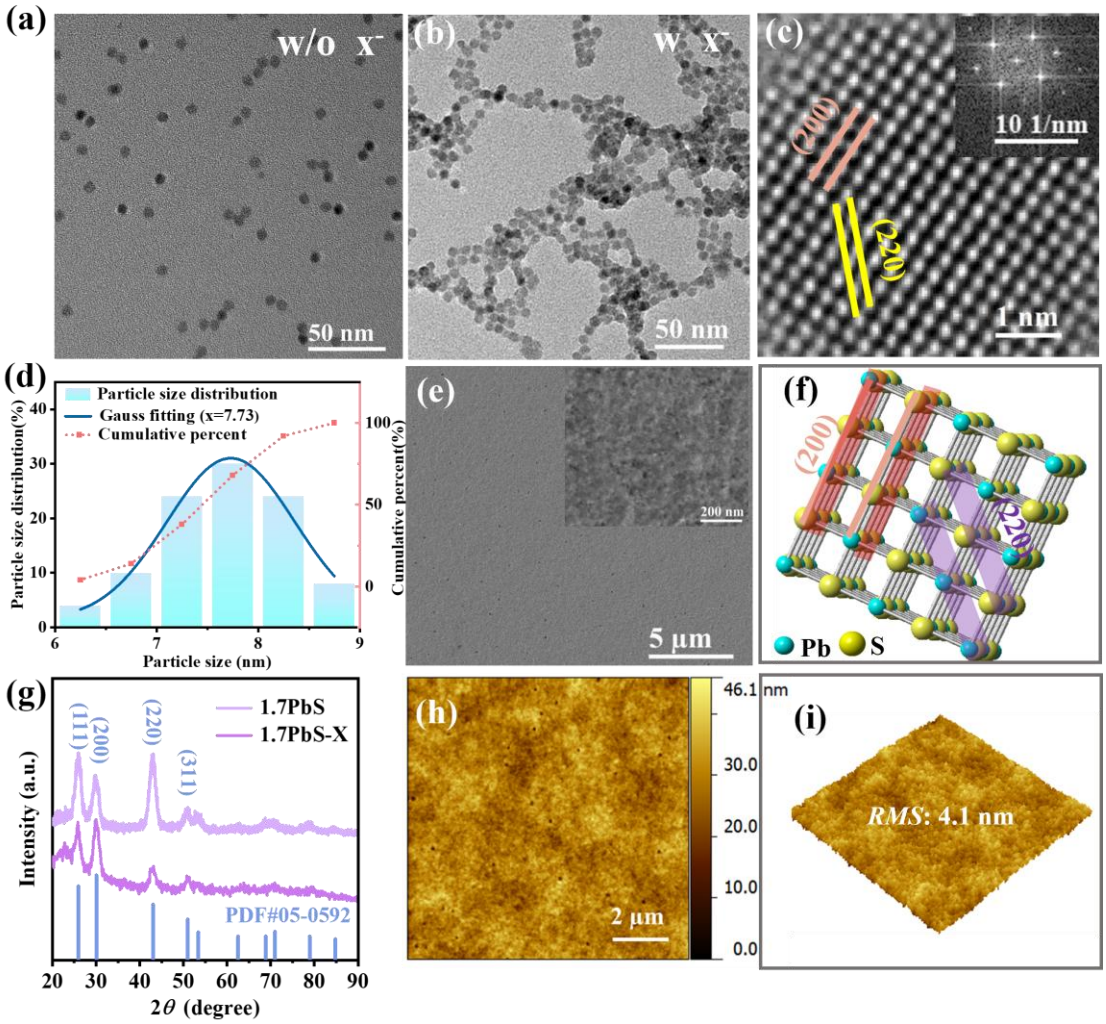

Fig. 1. Low-resolution TEM images of synthesized (a) 1.7PbS CQDs and (b) 1.7PbS-X. (c) High-resolution TEM image of a single 1.7PbS-X CQD (Inset: Electron diffraction pattern). (d) Particle size distribution of 1.7PbS CQDs. (e) SEM image of 1.7PbS-X CQDs film (Inset: magnified SEM image of 1.7PbS-X CQDs film). (f) Schematic diagram of PbS CQDs crystal structure. (g) XRD patterns of 1.7PbS CQDs and1.7PbS-X CQDs film. (h) AFM image of 1.7PbS-X CQDs film and (i) 3D representation of the image.

Absorption spectra for WO_x, ZnO, 0.9PbS-EDT and 1.7PbS-X are shown in Fig. 2(a). Both WO_x and ZnO are wide bandgap materials, demonstrating prominent absorption peaks predominantly within the UV range. Specifically, WO_x exhibits a

sharp absorption peak at 243 nm. Conversely, the first exciton absorption peak for 0.9PbS-EDT is located at 939 nm. The bandgap and particle size of the PbS CQDs can be deduced from the first exciton absorption peaks shown in Fig. 2(a). The bandgap of the CQDs with uniform size distribution can be calculated from the first exciton absorption peaks using Equation (1).

$$E_g = hc / \lambda \tag{1}$$

where E_g is bandgap energy, h is Planck's constant, c is speed of light, and λ is wavelength of incident light. The 0.9PbS-EDT has a bandgap of 1.32 eV, while the 1.7PbS-X has a bandgap of 0.73 eV. By substituting these bandgap values into Equation (2) [20], the particle size of the CQDs can be calculated corresponding to their exciton absorption peaks.

$$E_g = 0.41 + \frac{1}{0.0252d^2 + 0.0283d} \tag{2}$$

where E_g is bandgap energy and d is particle size of the quantum dot. Using Equation (2), the particle sizes of 0.9PbS-EDT and 1.7PbS-X are 6.1 nm and 9.5 nm, respectively.

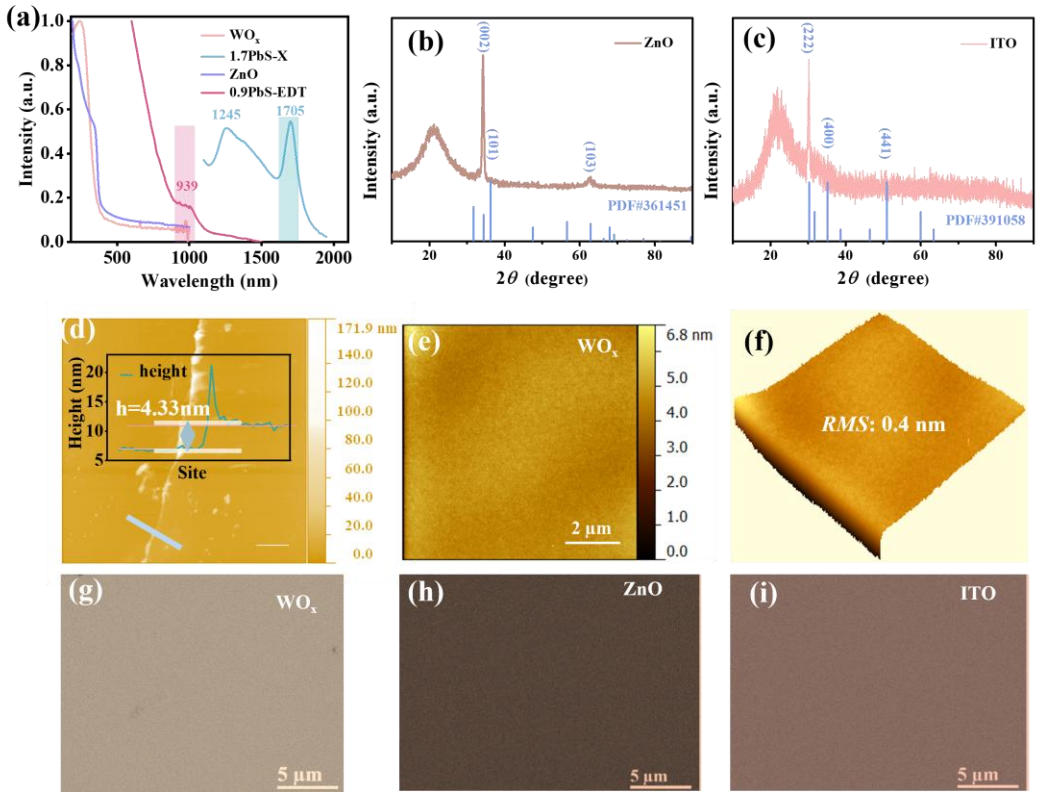

Fig. 2. (a) Absorption spectra of WO_x, ZnO, 0.9PbS-EDT and 1.7PbS-X. (b) XRD pattern of ZnO film. (c) XRD pattern of ITO film. (d) Thickness measurement of WO_x film using AFM image. (e) AFM image of WO_x film and (f) 3D presentation of the image. SEM images of (g) WO_x, (h) ZnO and (i) ITO films.

These calculated sizes are slightly larger than those determined statistically from the TEM images. However, it is evident that the bandgap decreases as the quantum dot size

increases.

Fig. 2(b) and (c) show the XRD patterns of magnetron-sputtered ZnO and ITO films on quartz substrates, respectively, with all peaks consistent with their standard PDF cards. Peaks marked with an asterisk belong to the quartz substrate used in the test. The absence of certain diffraction peaks in the XRD pattern is attributed to the preferential growth commonly observed in nanocrystalline thin-film materials. Our magnetron-sputtered ZnO thin films primarily exhibit a preferred orientation along the (002) direction. The thickness of the WO_x, as measured from the AFM image, is shown in Fig. 2 (d). Additionally, Fig. 2(e) and 2(f) display the AFM and 3D AFM images of the magnetron-sputtered WO_x film on quartz substrates, respectively, revealing a RMS surface roughness of 0.4 nm. SEM images of the WO_x, ZnO, and ITO films are shown in Fig. 2(g), (h), and (i), respectively.

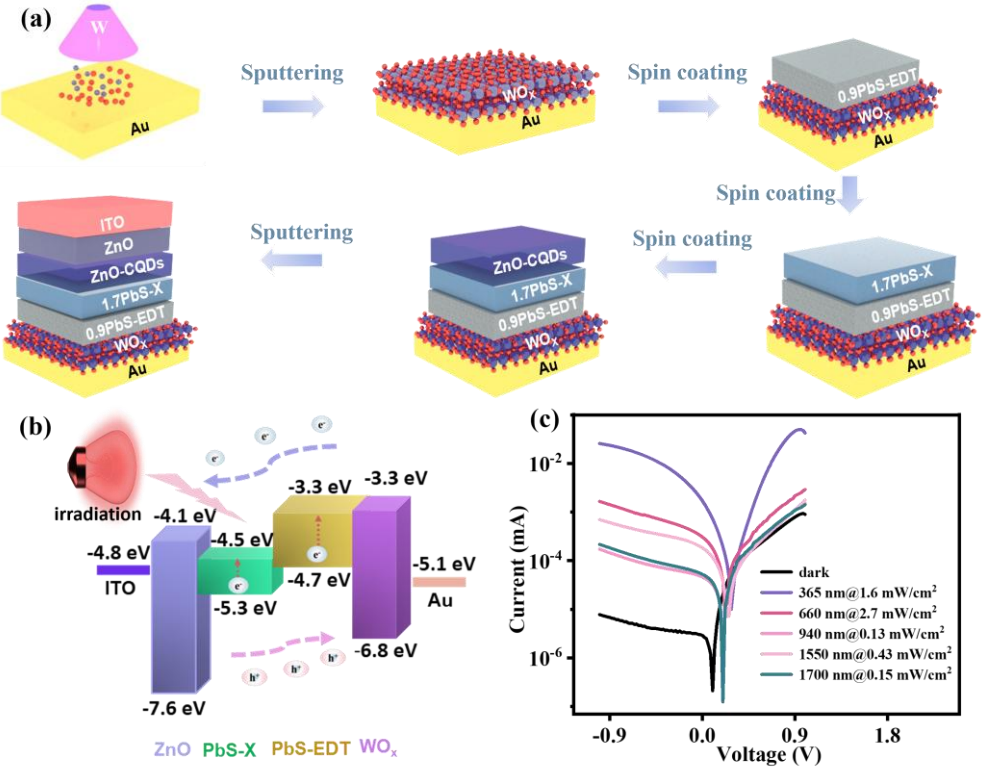

Fig. 3. (a) Schematic diagrams illustrating the fabrication process of the Au/WO_x/0.9PbS-EDT/1.7PbS-X/ZnO/ITO photodetector. (b) Energy band diagram of the photodetector under light conditions at 0 V. (c) Log *I-V* characteristics of the photodetector under dark and illumination.

The fabrication process of the Au/WO_x/0.9PbS-EDT/1.7PbS-X/ZnO/ITO photodetector is illustrated in Fig 3(a), and the processing steps are described in the experimental section. A novel secondary ligand mixed halogen solution-phase exchange method was introduced to effectively passivate large-size CQDs, hence significantly minimizing surface defects and enhancing device performance. Furthermore, ZnO-NPs were spin-coated over the CQDs film to protect it from sputtering damage, and an orthogonal solvent system was used to prevent dissolution damage to the underlying CQDs film during spin-coating. The energy band diagram of the photodetector is depicted in Fig 3(b). A photodetector comprising of p-i-n

heterostructure was designed and developed. ITO and Au are used as the top and bottom electrodes, respectively, with PbS CQDs as the light-absorbing layer, ZnO as the electron-transporting layer, and WO_x as the interface modification layer. The EDT ligand-exchanged 0.9PbS-EDT demonstrates weak p-type semiconductor characteristics, whileas the halogen ligand-exchanged PbS exhibits weak n-type semiconductor characteristics. These layers can be regarded as intrinsic light-absorbing layers. The p-i-n device structure facilitates the diffusion of electrons and holes upon contact due to the different types and concentrations of dopant atoms within the semiconductor. The diffusion of carriers generates a potential difference and electric field, forming a potential barrier across the p-i-n junction. Under dark conditions with forward bias, free electrons and holes diffuse towards the center of the p-i-n junction, thus effectively reducing the potential barrier height. When the potential barrier height is reduced sufficiently, the electrons and holes can traverse the p-i-n junction, hence a current is generated. Consequently, the resistance of the p-n junction decreases, leading to a linear increase in current through the junction. In reverse bias, the applied electric field counters the built-in electric field, causing electrons to drift from the p-region towards the n-region. However, due to the limited number of electrons in the p-region, this drift results in a weak current under dark conditions. As the reverse voltage increases, the reverse saturation current remains unchanged. Under illuminated conditions, photon energy can excite electrons within the i region of PbS, enabling them to transit from the valence band to the conduction band, thus generating electron-hole pairs. These photogenerated electrons drift towards n-ZnO, while holes drift towards p-0.9PbS-EDT, leading to the generation of photocurrent.

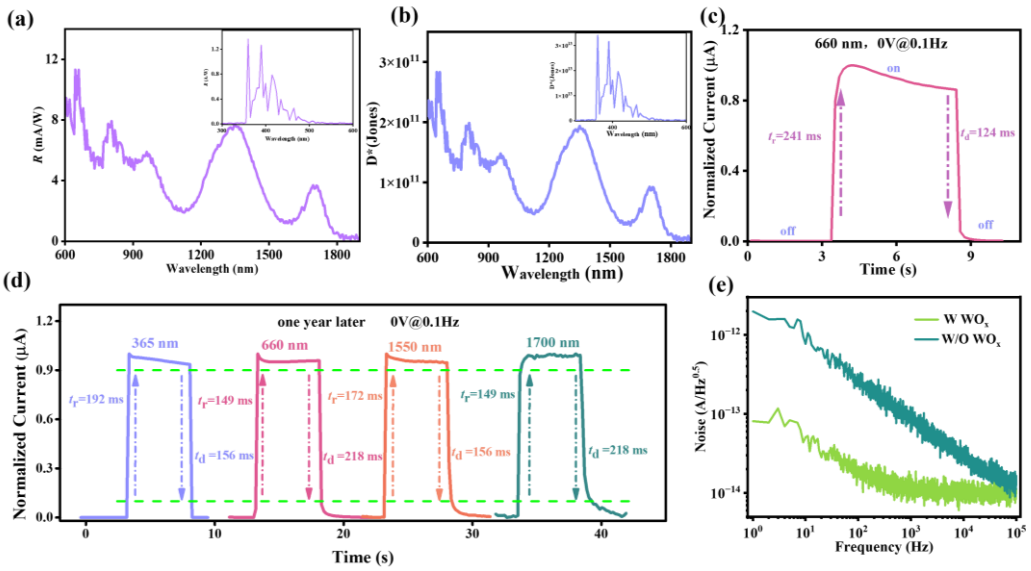

Fig. 4. Performance of the Au/WO_x/0.9PbS-EDT/1.7PbS-X/ZnO/ITO photodetector. The plots of (a) responsivity (*R*) and (b) detectivity (*D**) of the photodetector. (c) Transient photocurrent (TPC) of the photodetector under 660 nm illumination and (d) magnified TPC plot of the device at 0 V. (d) TPC plots across a broad wavelength range of 0.3-1.7 μm measured after the device was left in air for one year. (e) Noise power spectrum (i_n) of the photodetector under dark at 0 V.

The bandgap relationships for various samples can be calculated using the

empirical formula: $E_V = E_C + E_g$ (E_V: valence band maximum, E_C: conduction band minimum). Herein, the E_C and E_V of n-ZnO were obtained from the literature [21]. The E_g for both 0.9PbS-EDT and 1.7PbS-X were derived from calculated values based on the exciton absorption peaks. The $E_{VB,\ NHE}$ can be calculated using the formula [22]: $E_{VB,\ NHE} = \varphi + E_{VB,\ XPS} - 4.44$, where φ corresponds to work function of the instrument (4.2 eV). The measured $E_{VB,\ XPS}$ of 0.9PbS-EDT and 1.7PbS-X were 0.4 and 0.05 eV, respectively, from the XPS valence band (XPS-VB) spectra shown in Fig S1 and S2. Subsequently, the $E_{VB,\ NHE}$ of 0.9PbS-EDT and 1.7PbS-X were determined to be 0.16 and 0.77 eV, respectively. Utilizing the conversion relation: $E_{(vac)} = -4.5 - E_{VB,\ NHE}$, the E_V of 0.9PbS-EDT and 1.7PbS-X were -4.7 and -5.3 eV, respectively. The E_C for 0.9PbS-EDT and 1.7PbS-X were found to be -3.3 and -4.5 eV, respectively. Using UPS, the work function Φ of the sample can be calculated using the equation: $\Phi = h\nu - (E_{Fermi} - E_{cutoff})$, where $h\nu$ corresponds to He I energy (21.22 eV) [23]. This led to the determination of Φ for WO_x as 6.06 eV based on Fig S3, with its E_V determined as 6.8 eV. The E_g of WO_x can be derived from the absorbance results presented in Fig 2a and using the Tauc equation: $(\alpha h\nu)^2 = A(h\nu - E_g)$[24], where α is optical absorption coefficient associated with $h\nu$ and A is a constant. Fig. S4 indicates that the E_g of WO_x is 3.54 eV, resulting in E_C of -3.3 eV. Fig. 3(c) shows the log *I-V* characteristics of the photodetector under dark and illuminated conditions from -1 V to 1 V. Notably, when the device is at 0 V, photocurrent is generated under all light conditions, affirming the capability of the device to operate in self-powered mode. The dark current density of the device is 4.54 $nA \cdot cm^{-2}$ at -0.5V, which is well below the levels of most infrared photodetectors, indicating minimal noise level and suitability for focal plane arrays. Fig. s6 shows the log *I-V* characteristics of the photodetector without WOx as a control, and it is found that our addition of the WOx modification layer reduces the dark current by about an order of magnitude while ensuring that there is almost no decrease in the photocurrent of the device. Performance testing of the device under varying wavelengths of light across a wide spectrum from 0.36-1.7 μm revealed a large on/off ratio (I_{photo}/I_{dark}) of up to 3299. The results are shown in Table 1.

Table 1. Performances of the photodetector under various light wavelengths

Light wavelengths (nm)	Optical power density ($mWcm^{-2}$)	I_{photo}/I_{dark} -1 V bias	R (mAW^{-1}) 0 bias	D^* (Jones) 0 V bias
365	1.6	3299	104	2.59×10^{12}
660	2.7	213	11	2.83×10^{11}
940	0.13	22	5.4	1.34×10^{11}
1550	0.43	90	1.3	3.63×10^{10}
1700	0.14	28	3.5	8.68×10^{10}

Responsivity (R) and detectivity (D^*) are performance parameters for characterizing photodetector performance, and they can be calculated using the following equations [25]:

$$R = J_{ph} / P_{opt} \tag{3}$$

$$D^* = R\sqrt{A} / i_n \tag{4}$$

where J_{ph} is photocurrent density, P_{opt} is incident optical power, and i_n is dark current density. The R and D^* calculated using Equation (3) and (4), are presented in Fig. 4(a) and 4(b), respectively. By calculation, the R and D^* were 104 mAW^{-1} and 2.59×10^{12} Jones at -1 V under 365 nm illumination, respectively. Under 1700 nm illumination, the R and D^* were 3.5 mAW^{-1} and 8.68×10^{10} Jones at -1 V, respectively. Importantly, the D^* exceeded 10^{10} Jones across all tested wavelengths. The one cycle of transient photocurrent (TPC) curves measured under 660 nm illumination at 0 V are shown in Fig. 4(c). At this condition, the calculated rise time (τ_r) and decay time (τ_d) for the photodetector were 241 and 124 ms, respectively. The TPC curve obtained from testing at 0 V can also reveal the self-powered characteristic of the device. The TPC curves, over a wide spectrum of 0.3-1.7 μm, were measured after the device was exposed to air for one year, as presented in Fig. 4(d). It can be seen that the response times of the device remain in the same order of magnitude even after one year, hence showcasing the remarkable stability of the device. The noise power spectrum (i_n) of the photodetector under dark at 0 V were shown in Fig. (e), Test bandwidth Δf is 1 Hz. In commercial detectors, the noise current density at 500 Hz is typically used for comparison. Our device exhibits a noise current density of $1.2\times10^{-14}A/Hz^{0.5}$ at this frequency. With the insertion of a WO_x thin-film modification layer, the device's low-frequency noise was reduced by a factor of more than ten. This functional layer modified the interface between the electrode and the quantum dot thin-film layer, significantly reducing the noise generated by the device's ohmic contact.

4. Conclusion

In this work, we have pioneered a mixed-ligand solution-phase exchange strategy to address the long-standing challenge of {100} facet defect passivation in large-diameter PbS CQDs (exciton peak: 1.7 μm). This breakthrough enables the fabrication of high-quality infrared-active layers with ultralow trap densities. By integrating an atomic-scale WOx interfacial layer with energy-level-engineered transport layers (ZnO ETL and EDT-treated CQD HTL), we constructed a p-i-n heterojunction photodetector (Au/WOx/0.9PbS-EDT/1.7PbS-X/ZnO/ITO) that achieves record-low dark current densities (4.54 $nA\cdot cm^{-2}$ at -0.5 V). The device demonstrated high performance across a broad wavelength range of 0.36 to 1.7 μm, maintaining high values of D^* above 10^{10} Jones. Notably, even under illumination at 1.7 μm, the R and D^* reached 3.5 mAW^{-1} and 8.68×10^{10} Jones, respectively. These findings indicate that our WO_x-mediated interfacial control combined with mixed-halide passivation present a promising method for infrared photovoltaics. This new device structure, which exhibited ultralow dark current and high optical response, holds significant potential for future applications in next-generation focal plane array imaging.

CRediT authorship contribution statement

Qian Zhang: Investigation, Data curation, Software, Formal analysis, Writing – original draft, Writing – review & editing. **Libin Tang:** Conceptualization, Funding acquisition, Supervision, Resources, Validation, Methodology, Writing – review & editing. **Menghan Jia:** Writing – review & editing. **Liqing Yang:** Writing – review & editing. **Kar Seng Teng:** Writing – review & editing. **Yanfei Lü:** Conceptualization, Funding acquisition, Supervision, Validation, Writing – review & editing.

Declaration of Competing Interest

The authors declare that they have no known competing financial interests or personal relationships that could have appeared to influence the work reported in this paper.

Acknowledgments

This work was supported by the National Natural Science Foundation of China (Nos. 61106098 and 61965016); National Key Research and Development Program of China (2019YFB2203404); Yunnan Province Innovation Team Project (2018HC020) and Xingdian Talent Support Program for Young Talents of Yunnan Province.

Appendix A. Supplementary material

Supplementary data to this article can be found online at xxx.

References

[1] J. Liu, P.L. Liu, D.Y. Chen, T.L. Shi, X.X. Qu, L. Chen, T. Wu, J.P. Ke, K. Xiong, M.Y. Li, H.S. Song, W. Wei, J.K. Cao, J.B. Zhang, L. Gao, J. Tang, A near-infrared colloidal quantum dot imager with monolithically integrated readout circuitry, Nat. Electro. 5(7) (2022) 443-451.

[2] M. Sulaman, S. Yang, A. Bukhtiar, P. Tang, Z. Zhang, Y. Song, A. Imran, Y. Jiang, Y. Cui, L. Tang, B. Zou, Hybrid Bulk-Heterojunction of Colloidal Quantum Dots and Mixed-Halide Perovskite Nanocrystals for High-Performance Self-Powered Broadband Photodetectors, Adv. Funct. Mater. (2022).

[3] S.B. Hafiz, M. Scimeca, A. Sahu, D.K. Ko, Colloidal quantum dots for thermal infrared sensing and imaging, Nano Converg 6(1) (2019) 7.

[4] H. Seo, H.J. Eun, D. Choi, H.B. Na, Y. Shim, J. Heo, K.S. Cho, J.H. Kim, S.W. Kim, Cationic Molecular Metal Chalcogenide Ligand-Passivated Colloidal Quantum Dots and Their Application to Suppressed Dark-Current Near-Infrared Photodetectors, Adv. Mater. Tech. 8(11) (2023).

[5] Muhammad, D. Choi, D.H. Parmar, B. Rehl, Y. Zhang, O. Atan, G. Kim, P. Xia, J.M. Pina, M. Li, Y. Liu, O. Voznyy, S. Hoogland, E.H. Sargent, Halide-Driven Synthetic Control of InSb Colloidal Quantum Dots Enables Short-Wave Infrared Photodetectors, Adv. Mater. 35(46) (2023).

[6] C. Rosiles-Perez, M.A. Serrano-Estrada, S. Sidhik, A. Alatorre-Ordaz, A. Torres-Castro, M.A. Vallejo, A.E. Jimenez-Gonzalez, T. Lopez-Luke, Synthesis of high quality PbS colloidal quantum dots by ultrasonic bath as photosensitizers in a TiO2 solar cell, J. Solid State Chem. 292 (2020).

[7] W. Pan, M. Tan, Y. He, H. Wei, B. Yang, Organic Amine-Bridged Quasi-2D Perovskite/PbS Colloidal Quantum Dots Composites for High-Gain Near-Infrared Photodetectors, Nano Lett. 22(6) (2022) 2277-

2284.
[8] X.K. Yang, J. Yang, M.I. Ullah, Y. Xia, G.J. Liang, S. Wang, J.B. Zhang, H.Y. Hsu, H.S. Song, J. Tang, Enhanced Passivation and Carrier Collection in Ink-Processed PbS Quantum Dot Solar Cells via a Supplementary Ligand Strategy, ACS Appl. Mater. Interfaces 12(37) (2020) 42217-42225.
[9] M. Biondi, M.J. Choi, Z.B. Wang, M.Y. Wei, S. Lee, H. Choubisa, L.K. Sagar, B. Sun, S.W. Baek, B. Chen, P. Todorovic, A.M. Najarian, A.S. Rasouli, D.H. Nam, M. Vafaie, Y.G.C. Li, K. Bertens, S. Hoogland, O. Voznyy, F.P.G. de Arquer, E.H. Sargent, Facet-Oriented Coupling Enables Fast and Sensitive Colloidal Quantum Dot Photodetectors, Adv. Mater. 33(33) (2021).
[10] J.R. Yang, S.C. Lu, B. Xia, P.L. Liu, Y. Yang, Z.W. Xiao, J.B. Zhang, L. Gao, J. Tang, Excess PbBr2 Passivation of Large PbS Colloidal Quantum Dots to Reduce Dark-Current Density for Near-Infrared Detection, Phys. Rev. Appl. 19(1) (2023).
[11] J. Liu, P. Liu, T. Shi, M. Ke, K. Xiong, Y. Liu, L. Chen, L. Zhang, X. Liang, H. Li, S. Lu, X. Lan, G. Niu, J. Zhang, P. Fei, L. Gao, J. Tang, Flexible and broadband colloidal quantum dots photodiode array for pixel-level X-ray to near-infrared image fusion, Nat. Commun. 14(1) (2023).
[12] W.R. Wang, M. Zhang, Z.X. Pan, G.M. Biesold, S. Liang, H.S. Rao, Z.Q. Lin, X.H. Zhong, Colloidal Inorganic Ligand-Capped Nanocrystals: Fundamentals, Status, and Insights into Advanced Functional Nanodevices, Chem. Rev. 122(3) (2022) 4091-4162.
[13] Y. Kim, F.L. Che, J.W. Jo, J. Choi, F.P.G. de Arquer, O. Voznyy, B. Sun, J. Kim, M.J. Choi, R. Quintero-Bermudez, F.J. Fan, C.S. Tan, E. Bladt, G. Walters, A.H. Proppe, C.Q. Zou, H.F. Yuan, S. Bals, J. Hofkens, M.B.J. Roeffaers, S. Hoogland, E.H. Sargent, A Facet-Specific Quantum Dot Passivation Strategy for Colloid Management and Efficient Infrared Photovoltaics, Adv. Mater. 31(17) (2019).
[14] H. Beygi, S.A. Sajjadi, A. Babakhani, J.F. Young, F.C.J.M. van Veggel, Surface chemistry of as-synthesized and air-oxidized PbS quantum dots, Appl. Surf. Sci. 457 (2018) 1-10.
[15] E.M. Miller, D.M. Kroupa, J.B. Zhang, P. Schulz, A.R. Marshall, A. Kahn, S. Lany, J.M. Luther, M.C. Beard, C.L. Perkins, J. van de Lagemaat, Revisiting the Valence and Conduction Band Size Dependence of PbS Quantum Dot Thin Films, Acs Nano 10(3) (2016) 3302-3311.
[16] M.S. Martinez, A.J. Nozik, M.C. Beard, Size-Dependent Janus-Ligand Shell Formation on PbS Quantum Dots, J. Phys. Chem. C 125(39) (2021) 21729-21739.
[17] J.Z. Fan, N.T. Andersen, M. Biondi, P. TodoroviC, B. Sun, O. Ouellette, J. Abed, L.K. Sagar, M.J. Choi, S. Hoogland, F.P.G. de Arguer, E.H. Sargent, Mixed Lead Halide Passivation of Quantum Dots, Adv. Mater. 31(48) (2019).
[18] Y. Xia, S. Liu, K. Wang, X. Yang, L. Lian, Z. Zhang, J. He, G. Liang, S. Wang, M. Tan, H. Song, D. Zhang, J. Gao, J. Tang, M.C. Beard, J. Zhang, Cation-Exchange Synthesis of Highly Monodisperse PbS Quantum Dots from ZnS Nanorods for Efficient Infrared Solar Cells, Adv. Funct. Mater. 30(4) (2020).
[19] Q. Xu, I.T. Cheong, H. Song, V. Van, J.G.C. Veinot, X. Wang, Heterogeneous Integration of Colloidal Quantum Dot Inks on Silicon Enables Highly Efficient and Stable Infrared Photodetectors, Acs Photonics 9(8) (2022) 2792-2801.
[20] I. Moreels, K. Lambert, D. Smeets, D. De Muynck, T. Nollet, J.C. Martins, F. Vanhaecke, A. Vantomme, C. Delerue, G. Allan, Z. Hens, Size-Dependent Optical Properties of Colloidal PbS Quantum Dots, Acs Nano 3(10) (2009) 3023-3030.
[21] A. Chiu, C. Lu, D.E. Kachman, E. Rong, S.M. Chintapalli, Y. Lin, D. Khurgin, S.M. Thon, Role of the ZnO electron transport layer in PbS colloidal quantum dot solar cell yield, Nanoscale 16(17) (2024) 8273-8285.
[22] X. Li, B. Kang, F. Dong, Z. Zhang, X. Luo, L. Han, J. Huang, Z. Feng, Z. Chen, J. Xu, B. Peng, Z.L.

Wang, Enhanced photocatalytic degradation and H_2/H_2O_2 production performance of S-pCN/$WO_{2.72}$ S-scheme heterojunction with appropriate surface oxygen vacancies, Nano Energy 81 (2021).
[23] X. Zou, Y. Dong, J. Ke, H. Ge, D. Chen, H. Sun, Y. Cui, Cobalt monoxide/tungsten trioxide p-n heterojunction boosting charge separation for efficient visible-light-driven gaseous toluene degradation, Chem. Eng. J 400 (2020).
[24] J. He, X. Zhou, Y. Wang, M. Yuan, H. Xia, X. Chen, Y. Ge, X. Wang, L. Gao, J. Tang, Mid-infrared response of PbS colloidal quantum dot solids, J. Mater. Chem. C 11(29) (2023) 10033-10042.
[25] Y. Fang, A. Armin, P. Meredith, J. Huang, Accurate characterization of next-generation thin-film photodetectors, Nat. Photon. 13, (2019) 1–4.

Supporting Information

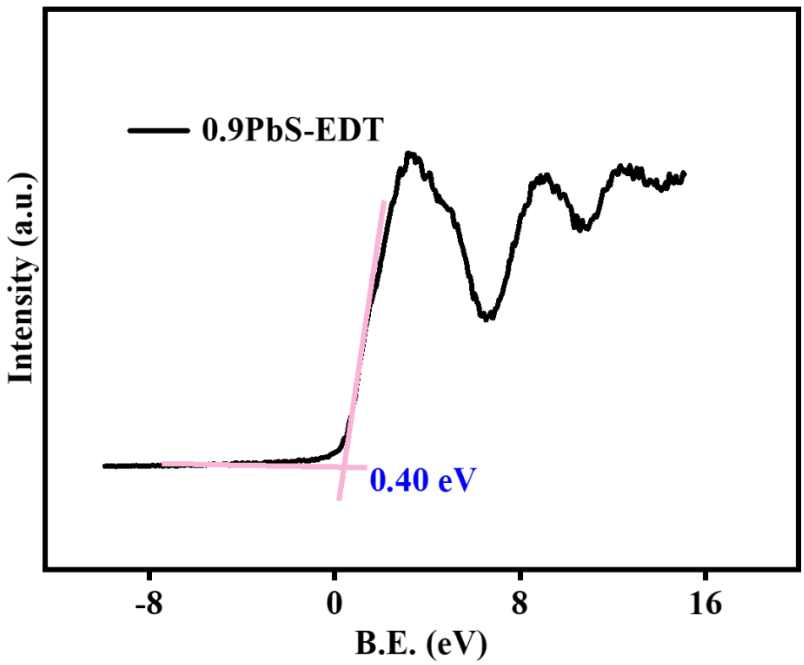

Fig S1 XPS-VB spectrum of 0.9PbS-EDT

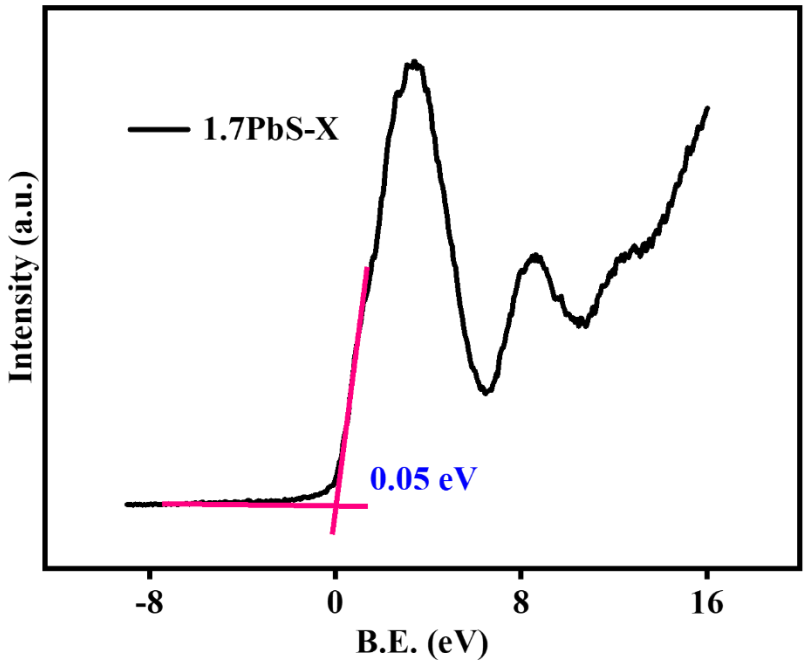

Fig S2 XPS-VB spectrum of 1.7PbS-X

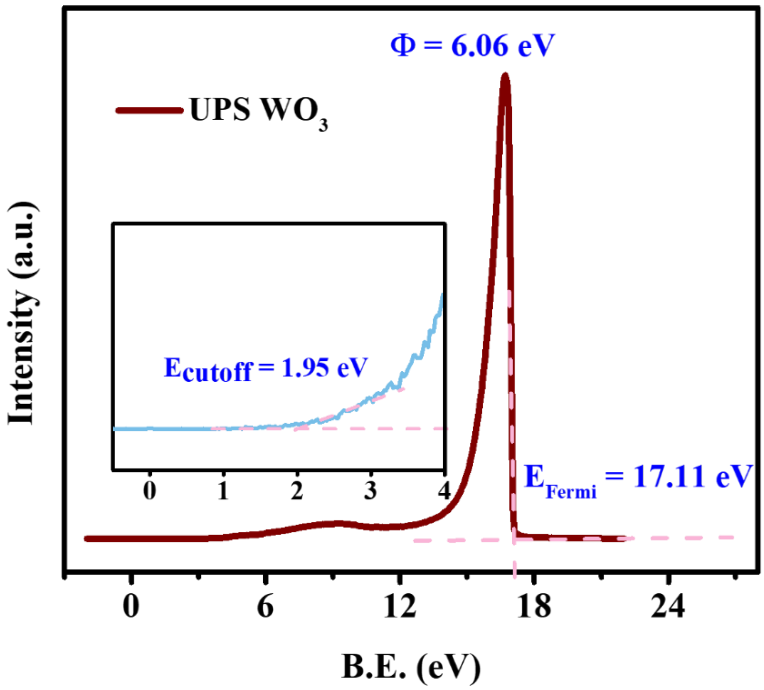

Fig S3 UPS spectra of WO_x

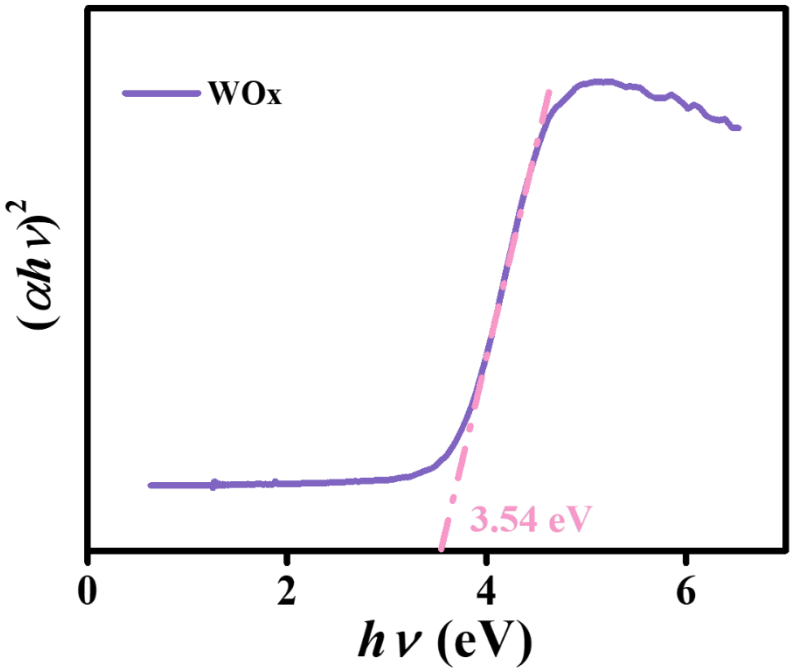

Fig S4 Plot of $[\alpha(h\nu)]^2$ versus photon energy

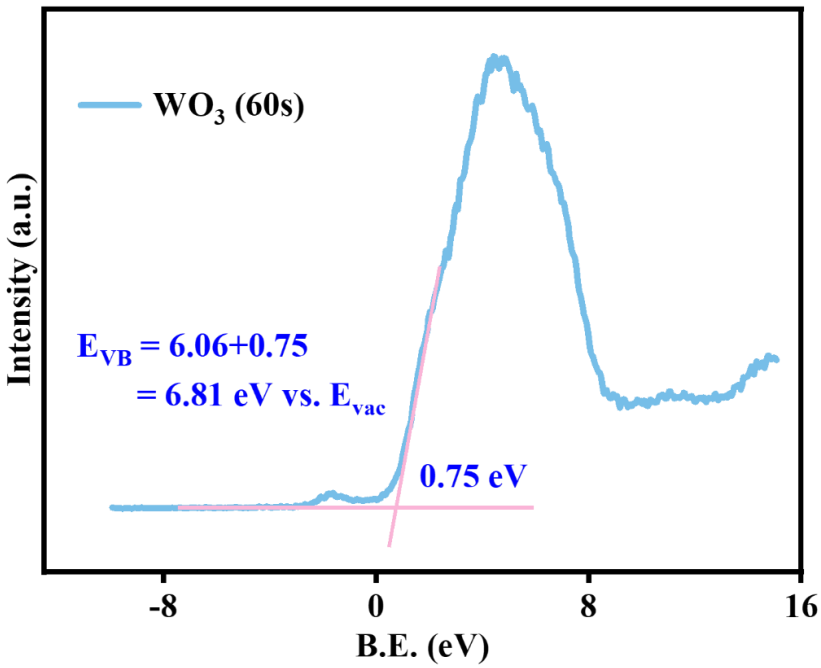

Fig S5 XPS-VB spectrum of WO_x

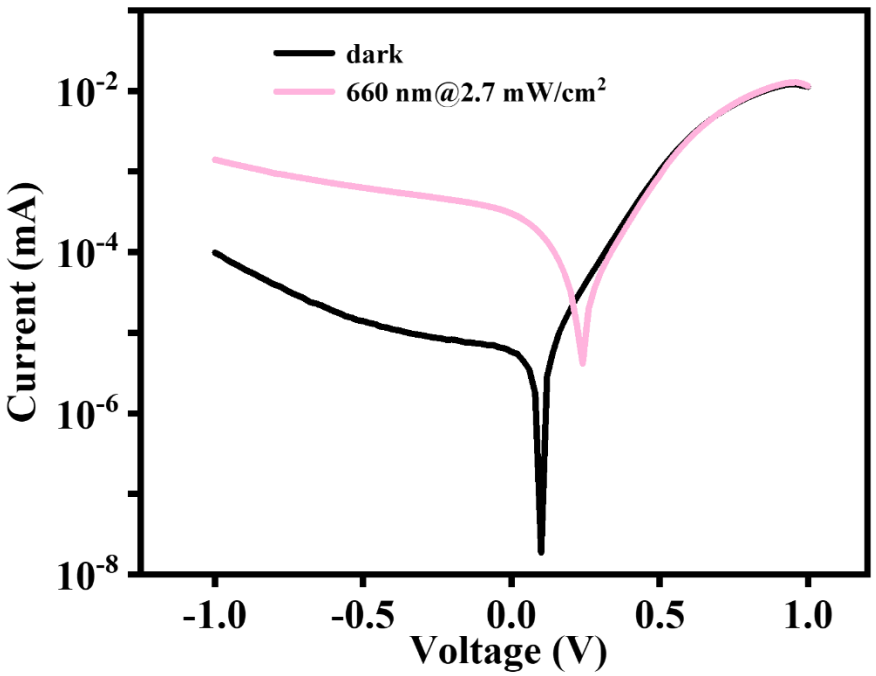

Fig S6 Log *I-V* characteristics of the photodetector without WO_X under dark and illumination.

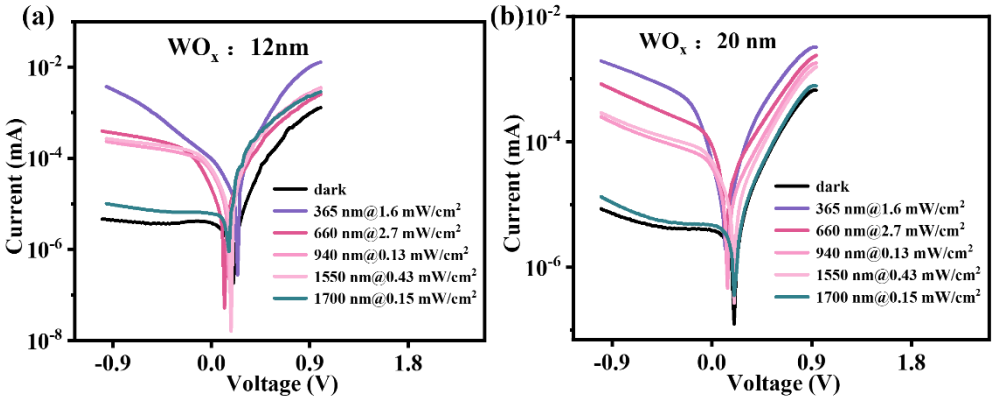

Fig S7 log *I-V* characteristics of the photodetector with thicker WO_X, (a) WO_x films at 12 nm thickness and (b) WO_x films at 20 nm thickness

Table S1. Performances of the photodetector under various light wavelengths at -1 V bias.

Light wavelengths (nm)	Optical power density ($mWcm^{-2}$)	WOx : 4.3 nm I_{photo}/I_{dark}	WOx : 12 nm I_{photo}/I_{dark}	WOx : 20 nm I_{photo}/I_{dark}
365	1.6	3299	826	228
660	2.7	213	84	98
940	0.13	22	51	29
1550	0.43	90	59	33^0
1700	0.14	28	2	1.6
Dark current density -0.5 V	0	4.54 nA • cm^{-2}	4.09 nA • cm^{-2}	5.02 nA • cm^{-2}